Quasi-optic synthetic phased-array terahertz imaging

John O'Hara and D. Grischkowsky

School of Electrical and Computer Engineering, Oklahoma State University, Stillwater, Oklahoma 74078

Received August 13, 2003; revised manuscript received February 17, 2004; accepted February 24, 2004

A quasi-optic terahertz (THz) imaging system that utilizes optoelectronic methods for pulsed THz generation and reception and optical methods for image formation is demonstrated and theoretically explained. The system can be used to produce coherent, field amplitude, and energy density images with diffraction-limited resolution in two transverse dimensions. Simultaneous bandwidth-limited resolution is achieved in the depth dimension by means of the ranging capabilities of the system. The system is shown to accurately produce images of several objects to verify diffraction-limited imaging. Imaging power is extended by aperture synthesis to result in transverse resolution the order of a wavelength. Several individual, coherent images are recorded, each synthetically appearing to be formed by a different element of an optical phased array. The multiple images are simply superposed to create a higher-resolution image. Theoretical calculations fully describe the broadband imaging and include aberration and diffraction effects to further verify system performance. Calculated images are a good match with experimental results. © 2004 Optical Society of America

OCIS codes: 110.5100, 250.0250, 320.0320.

1. INTRODUCTION

History has shown that, whenever a portion of the electromagnetic spectrum becomes practically usable, it is soon adapted to an imaging configuration. Such is the case for the terahertz (THz) band that, over the past couple of decades, has been made available by optoelectronic[1,2] and electro-optic,[3,4] techniques. Imaging with optoelectronically generated THz is promising because of its large number of attractive properties. Generated in the form of broadband (typically 0.05–2.5 THz), coherent, transform-limited pulses,[5] this THz radiation can be used to probe material properties simultaneously, such as the complex dielectric function, over a large bandwidth. These pulses can also be used in a radar configuration whereby ranging or echolocation techniques can reveal the three-dimensional (3-D) spatial structure of an object.[6] Furthermore, coherence permits aperture synthesis, a powerful resolution-increasing tool for any imaging system.[7] With its relatively short wavelength (0.12–6 mm), THz radiation is naturally suited for imaging with resolution on the order of a few hundred micrometers. Finally, many materials exhibit unique properties within the THz region. For example, THz is highly sensitive to water and other polar compounds[8–10] that are often strongly absorptive. On the other hand, many visually opaque and, in fact, most dry, nonpolar, nonmetallic items such as plastic, paper, glass, and cardboard, are quite transparent to THz.[11]

Several types of THz imaging systems already exist, all having different meritorious properties. One such system uses a tightly focused THz beam through which a thin, uniform sample is raster scanned. Either the transmitted[12] or reflected[13] THz beam is measured point by point to build up the image. This system achieves a good signal-to-noise ratio (SNR) due to the high brightness of the illumination point but requires a sample to be thin and uniform to stay within the Rayleigh range of the beam. Impulse imaging systems[6] use radar principles to build up an image from the time-delayed THz pulses scattered off some object. Such systems can achieve good range and cross-range (transverse) resolution, in a single direction, by means of synthetic aperture techniques. High cross-range resolution is more difficult to achieve in two dimensions because of the necessarily more complicated object rotations. Also, this technique uses a single receiver to incrementally sample a small portion of the scattered wave front making it difficult to achieve a good SNR. Electro-optic THz imaging systems[14,15] can be used in conjunction with CCD cameras to form whole images at once, thus greatly accelerating the imaging process. However, this speed generally comes at the cost of dynamic range, thus reducing the ability of the system to measure weakly reflecting or small objects.

Here we review an existing THz imaging system[7,16] and present new experimental and theoretical results obtained from it. This system retains many of the beneficial features of previous systems but also adds powerful features that increase functionality. In Section 2 we review the experimental setup of the quasi-optic imaging system, and in Section 3 we show a recorded image that defines the system's point-spread function (PSF) or spatial impulse response. In Section 4 we explain a powerful extension of the work called synthetic phased-array THz imaging wherein we use aperture synthesis (AS) to record many separate images and then superpose them to form a higher-resolution image. New experimental results demonstrate the system's full 3-D capabilities and are also described in detail in Section 4. Section 5 contains the first presentation of the theoretical analysis of this system along with comparisons to experimental data, which show good agreement. Finally, in Section 6 we present some brief conclusions.

0740-3224/2004/061178-14$15.00

2. EXPERIMENTAL SETUP

Figure 1 shows the quasi-optic THz imaging system. THz production begins at the transmitter, shown in Fig. 2(a), where a train of 80-fs optical pulses having a center wavelength of 801 nm and an average power of 25 mW are shaped into an elliptical focus that lies parallel to and illuminates the anode line of a coplanar transmission line on a semi-insulating GaAs chip.[17] The elliptical focus permits the use of higher optical power to enhance THz emission, while maintaining sufficiently low optical fluence to prevent damage to the chip. The two coplanar lines are 10 μm wide, separated by 80 μm, and run in the $\pm y$ directions, perpendicular to the linear optical field polarization. The transmission line is biased at 55 V so that the free carriers generated by the optical pulses accelerate and radiate. Like the incident optical radiation, the resulting THz radiation is linearly polarized in the xz plane, perpendicular to the coplanar lines. Much of this THz is collected by a 10-mm-diameter, hyperhemispherical lens made of high-resistivity ($>10^4 \Omega$ cm) silicon and attached to the back of a GaAs chip. Using this lens, the transmitter emits a collimated train of subpicosecond pulses of THz radiation. These pulses are directed and weakly focused onto the object by a paraboloidal mirror, a flat mirror, and a high-resistivity silicon lens, located at its focal length ($f = 280$ mm) upstream from the object. This forms an illumination spot, linearly polarized in the xz plane, with a frequency-independent $1/e$ amplitude diameter of approximately 14 mm on the object. Experimental results and Gaussian beam propagation calculations confirm that, because of weak focusing and the small area over which the beam is used, the illumination is effectively planar, varying by only $\lambda/20$ over the beam profile at 0.7 THz. The object scatters a portion of the incident radiation to a 152-mm-diameter spherical mirror positioned at twice its focal length ($f = 305$ mm) from the object. In this configuration, the mirror forms a real, one-to-one inverted image of the object 17 mm in front of the fixed THz receiver. The Fig. 1 inset shows a close-up view of the object, represented by a ball in the figure. The object can be scanned in the x or y direction and can be positioned anywhere in the xy plane. Because of the one-to-one imaging configuration, object translation results in one-to-one image translation, whereby the image is moved in front of and sampled by the fixed receiver.

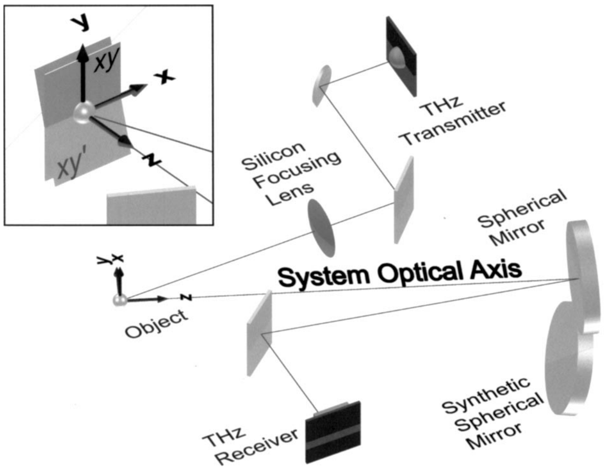

Fig. 1. Quasi-optic THz imaging system. The line shows the THz path through the system. The inset shows a close-up view of the object and scan planes.

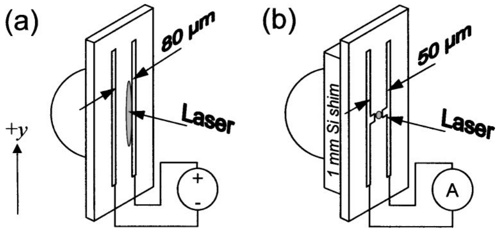

Fig. 2. THz (a) transmitter and (b) receiver.

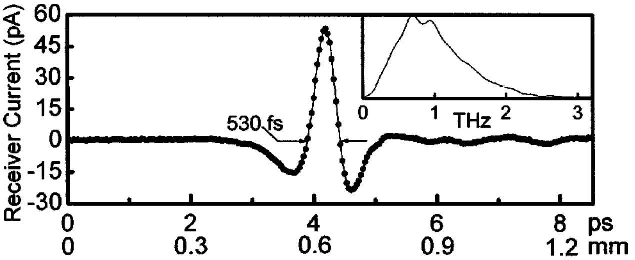

Fig. 3. Single measured spatial sample of a THz image. Inset shows the normalized amplitude spectrum. Time axis (in picoseconds) can be translated to depth (in millimeters) because of the ranging configuration.

The receiver consists of a 10-mm hyperhemispherical silicon lens attached to a shimmed, 500-μm-thick silicon-on-sapphire chip upon which lies a 50-μm polarization-sensitive dipole antenna, as shown in Fig. 2(b). The 1-mm silicon shim between the silicon-on-sapphire chip and the silicon lens places the focus of the lens 1 mm in front of the dipole antenna and places the antenna itself in a new conjugate imaging plane to the image plane formed by the spherical mirror 17 mm in front of the receiver. Therefore, this arrangement forms a secondary imaging system wherein the image formed by the spherical mirror is again optically imaged with demagnification onto a new image plane containing the sampling antenna. With the secondary THz image projected onto it, the dipole antenna is photoconductively switched by another 80-fs optical pulse, split from the first and appropriately delayed in time. The receiver optical pulse train has an average power of 11 mW and is focused onto the 5-μm gap between the poles of the antenna. Each pulse produces free carriers that generate a dc current proportional to the instantaneous electric-field amplitude of the component of the THz pulse linearly polarized in the xz plane. By measuring this current while changing the relative delay between the detected THz pulse and the optical gating pulse, the entire time-dependent electric field of the THz pulse can be recorded. Several of these measurements are collected with the object in various positions to build up an image, point by point.

Image recording proceeds as follows. The object is fixed at some position (x, y) and then the receiver records a time-domain measurement $E(t)$, a single spatial sample of the image. This is a current versus time-delay measurement, where the measured current is proportional to the electric-field amplitude. One such measurement and its spectrum are shown in Fig. 3. Following this measurement, the object (and correspondingly the image) is moved to a new position and then fixed. Again, a single time-domain measurement is recorded. This process is repeated until the entire image is sampled. The resulting electric-field data set is three dimensional with two transverse dimensions and one temporal dimension or $E(x, y, t)$. Because of the ranging nature of the system, the temporal dimension can also be directly translated to spatial depth information, taking into account the round-trip travel time of the THz pulse scattered from the object. The data form then becomes $E(x, y, z)$, where $z = t \times (0.150 \text{ mm/ps})$.

The general layout of the system is designed to minimize third-order aberrations, in particular, astigmatism. To this end, the central axis of the scattered THz path (system optical axis) subtends only 10° as it is reflected from the spherical mirror. This tight path folding reduces the off-axis nature of the system as much as possible without clipping the scattered THz wave front on other system components. The illumination axis and system optical axis subtend 17° at the object.

The object is mounted on the tip of a pyramid-shaped paraffin wax holder, which is essentially invisible because of its stealthy shape and low refractive index (~1.6 over the bandwidth). The holder's pyramid shape points toward the THz source, so that radiation that does strike the holder is reflected away from the spherical collection mirror. To mitigate the strong absorption that is due to water vapor,[10] the entire system was enclosed in an airtight box that was purged with dry air during data collection.

The advantages of this system are significant. First, the spherical imaging mirror has a large collection aperture that makes possible imaging of small or weakly reflecting objects without a detrimental loss of SNR. Additionally, the large extent of the mirror enables it to form an image automatically with good resolution, without the need for mathematical reconstruction or deconvolution techniques. Further, the system can also image large or complex objects just as easily as small ones. The system also performs simultaneous range and transverse (cross-range) imaging, thus obtaining 3-D data. Since imaging is done optically, many well-known image-processing tools can be readily adapted to the system. Finally, since it is a coherent system, resolution can be further increased by aperture synthesis.

3. QUASI-OPTIC IMAGING RESULTS

To determine the resolving power of the system, we imaged a single, 1-mm-diameter chrome-plated steel ball. Only a small solid angle portion of the ball scattered radiation to the spherical mirror; therefore it behaved as a point source. Since the system was well corrected, the image resolution was limited by diffraction, not aberrations, thus providing a measure of the diffraction limitation of the system. This image also defined the broadband PSF of the system.

In our initial measurements the recorded image contained only one transverse dimension, obtained by scanning the object in the x direction alone. The image consisted of 41 spatial samples each spaced by 150 μm thereby covering a range from $x = -3$ to 3 mm. Each spatial sample was an 8.5-ps time-dependent waveform consisting of 256 data points, each separated by 33.3 fs. The peak SNR was approximately 95. Figure 4 shows two views of the resulting image. Since the range resolution is much better than the transverse spatial resolution, the image takes on a fin shape lying at some angle with respect to the x axis. The angled orientation, apparent in Fig. 4(a), is due to the angled illumination. As the object moves in x, the THz path length between the transmitter and object changes, thus causing different arrival times for the illuminating pulses. Figure 4(b) shows a transverse view of the object wherein the transverse spatial resolution can be determined.

The spatial resolution can be quantified by use of a full width at half-maximum measurement of the image, similar to the Buxton resolution criterion.[18] This measurement is 1.8 mm. Even though the image was formed optically, the THz system can, unlike most optical systems, resolve objects in range by use of pulsed radiation in a radar fashion. The resulting range resolution can be calculated with the formula $c\tau/2$, where c is the speed of light

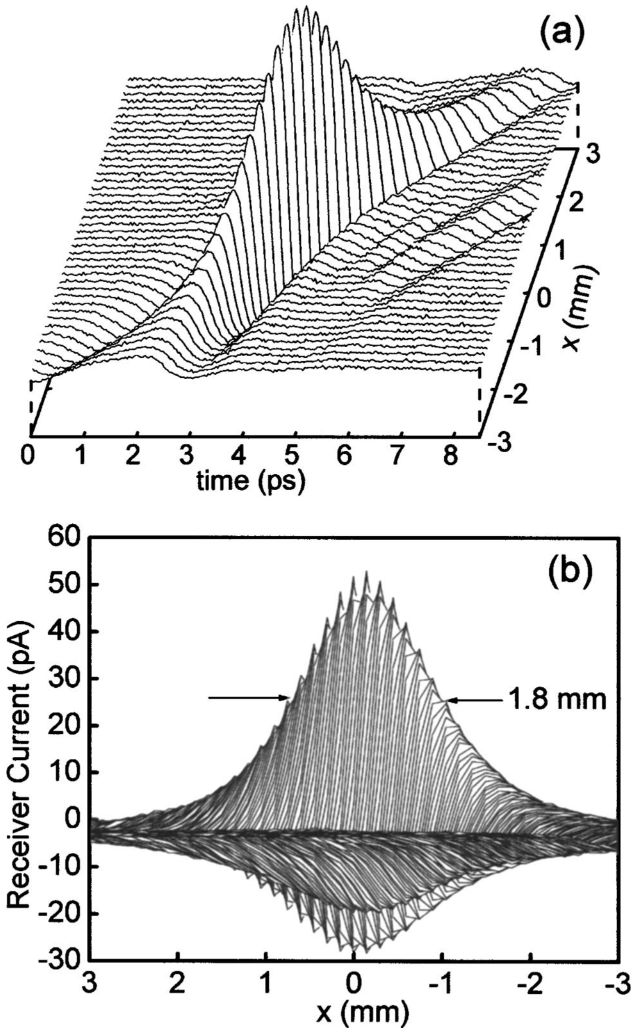

Fig. 4. Measured THz image of a 1-mm steel ball (point source): (a) plot comprised of a set of curves constant in x and (b) side view of plot comprised of a set of curves constant in time.

in free space and τ is the width of the THz pulse at its zero crossings. In this case, two reflected pulses are deemed temporally resolved when their main lobes do not overlap with each other, similar to the Schuster criterion.[18] Using $\tau = 530$ fs, the resulting range resolution is 80 μm. Since the system is well corrected, these two values, 1.8 mm and 80 μm, define the diffraction-limited resolution of the system.

Other resolution criteria have also been successfully applied to THz imaging systems. Range resolution in particular has been quantified by many different criteria, such as the Rayleigh[13] or Sparrow[19] criterion. Interferometric techniques have also been used to resolve objects separated by only approximately 10 μm in range[20] and to measure thin dielectric films.[21] Although interferometry could not be used in our THz system, other range resolution criteria could have been applied and would have yielded somewhat better range resolution values. Clearly, the choice of resolution criteria depends on the type of imaging system and the form and complexity of the received data. The criteria used in this work were chosen for their ease of application to the image data and to ensure conservative resolution results in more complicated objects.

To determine if the system was indeed well corrected and operating in the diffraction limit, another image was taken after halving the diameter of the spherical mirror, which is the most limiting aperture in the system.[22] An annular absorber, made of woven graphite cloth, was placed over the mirror surface to halve its diameter. The absorber had a 76-mm-diameter hole cut from its center so that only the THz that struck the outside annulus of the mirror was absorbed. The resulting image generated in this configuration had an increased transverse spatial extent of 3.1 mm, a 1.72 times increase in size. The range resolution was unchanged, as expected, and the peak SNR was reduced to approximately 30.

The change in spatial resolution was not exactly proportional to the two times decrease in aperture size. This deviation is due to the fact that the system is broadband and the various frequency components interfere with each other to change the extent of the final image. In fact, the 1.72 times increase in spatial extent agrees almost exactly with broadband theoretical predictions. Consequently, the system was indeed operating within the diffraction limit of the spherical imaging mirror.

4. SYNTHETIC PHASED-ARRAY IMAGING

The next logical step for improving the quasi-optic THz imaging system was to increase its resolving power. This was accomplished by AS, a means by which the resolution-defining aperture in the system is synthetically increased in transverse extent. Radio astronomers began using this powerful technique to increase the resolving power of their telescopes over 40 years ago[23] and continue to do so today.[24,25] Approximately 30 years ago Labeyrie advanced such ideas to the optical realm when he used two independent optical telescopes to perform stellar interferometry.[26] His work set the foundation for more complicated optical AS. Since then, AS has been implemented in ground-based optical astronomy[27] and can yield images with resolution unobtainable by even space-based telescopes.

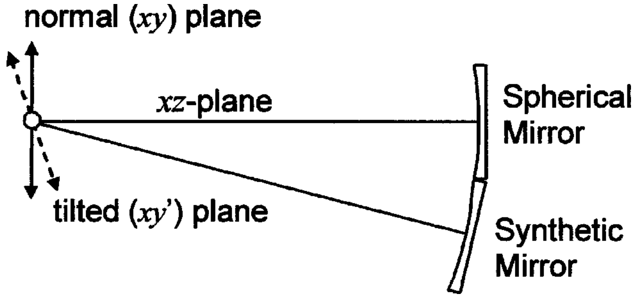

Fig. 5. Side view of the phased-array THz imaging system. Normal and tilted scan planes are shown as solid and dotted lines, respectively.

Today, AS is commonly used to generate high-resolution images at microwave frequencies, a practice known as synthetic aperture radar (SAR). Other forms of imaging use inverse SAR principles[28,29] or deconvolution methods and some have already been adapted to THz imaging systems.[6,19,30] Still, AS is not a usable method for every application. In particular, optical AS is difficult to use because of the strict phase relationships that must be maintained.

Because of its coherent nature and relatively long wavelengths, compared with optical fields, THz systems are prime candidates for AS. For the quasi-optic THz imaging system, AS was the ideal method by which the aperture extent could be increased. Other possible methods, such as adding more spherical mirrors into the system or increasing the size of the existing mirror, were also considered but were found unusable for several reasons. For example, adding another spherical mirror in the system requires impracticably difficult alignment and positioning of both mirrors. Similarly, implementing a larger spherical mirror requires a complete redesign of the layout of the system to avoid clipping the THz beam. Both solutions also aggravate imaging aberrations.

Aperture synthesis, on the other hand, allows another mirror to be synthetically added into the system with no adverse effects to imaging. In Fig. 1 the system shows a synthetic spherical mirror located below the original. This mirror effectively shares a common center of curvature with the real mirror such that the two essentially form a single, larger, sparse-aperture optic. We note that imaging is accomplished by scanning the object in the xy plane. The xy plane, however, appears tilted from the vantage of the synthetic mirror. With this realization, we find that the real mirror can be made to see the object from the vantage of the synthetic mirror by simply tilting the scan plane by the amount equal to the angular separation between the mirrors. The Fig. 1 inset shows this tilted plane, labeled xy'. Figure 5 illustrates this principle in more detail. By tilting the scan plane, the real spherical mirror can be used to implement a synthetic spherical mirror. Each mirror, therefore, becomes a single element of a synthetic phased array and both have a known spatial relationship with each other. Hence, the procedure is termed synthetic phased-array THz imaging.

The procedure for synthetic phased-array imaging is as follows. First, an image is recorded with the object and scan plane fixed in the normal configuration shown as the *xy* plane in Figs. 1 and 5. After recording, the scan plane is tilted by some desired amount and locked in the new position. This gives the real spherical mirror the vantage of the synthetic mirror. Another image is recorded as before with the real spherical mirror. Because of the tilt, the resulting image appears to have been formed by the synthetic mirror. In this way multiple images are recorded, each appearing to have been formed by a different mirror in the system. Additional details with regard to the formation and orientation of the synthetic mirrors and their images can be found in Ref. 22.

Since the scan plane can be continuously tilted about either or both the *x* or the *y* axis, many such images can be recorded with arbitrary positioning of mirrors. Mirrors can even be positioned such that their extents overlap, thus filling in the aperture more fully. Since each mirror is an element of a phased array, each individual image is an independent image formed by a single element of that array. By their judicious placement, the synthetic mirrors essentially act in unison as one large, sparse-aperture optic. Furthermore, all the phase information necessary for proper interference is contained in the electric-field image data. Therefore, the independent, coherent images formed by each mirror can simply be numerically superposed to yield the single higher-resolution image that would be formed if the larger aperture were actually implemented.

For successful AS, however, all the coherent THz images must be locked in a known phase relationship. This phase relationship is established by ensuring that the origin for all the scan planes is common. The Fig. 1 inset shows the object at this origin and how the scan planes share this common point. Therefore, when the object is at the origin it is at the same absolute, 3-D spatial position regardless of scan plane orientation. Each image contains a waveform (a spatial sample) that corresponds to the object positioned at the origin and, because the origin is common, each origin waveform should overlap exactly in time, assuming the object is a point source. Figure 6 shows two such overlapping waveforms taken from two images of the 1-mm ball (point source). One waveform was recorded with the scan plane in the normal configuration (0° tilt) and the other with the scan plane tilted −16° about the *x* axis. The close overlap between the two waveforms ensured that the images and, therefore, the phased-array elements shared a common origin and had a known phase relationship.

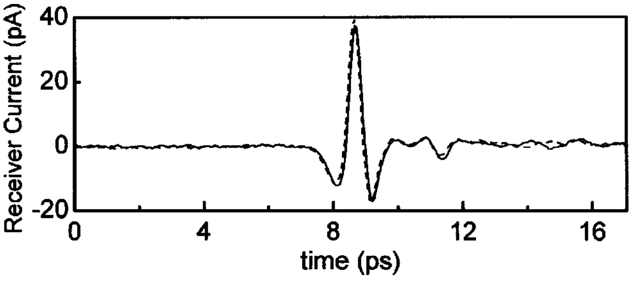

Fig. 6. Time overlap of two measured phase reference waveforms, dashed and solid curves, for different scan plane orientations.

For this method of phase referencing to work, the placement of the object must be accurate. Transverse placement is done by aligning the object with the cross hairs of a long-distance microscope mounted on a fixed kinematic base. The microscope observes the object along the system optical axis (in the $-z$ direction) so that the cross hairs register the *x* and *y* object positions. This results in a transverse placement accuracy of approximately 15 μm; more than required as shown by the following spatial frequency calculation. If φ is the full angular extent of the mirror subtended at the axial image point, then the highest angular spatial frequency possible in the image is $k_y = 2\pi \sin(\varphi)/\lambda = 12.89\ \mathrm{mm}^{-1}$, where $\varphi = 14.25°$ and λ is 120 μm corresponding to 2.5 THz. By use of this value, the shortest spatial wavelength generated by the system in a normal configuration is $\lambda_y = 2\pi/k_y = 488\ \mu$m; over 30 times larger than the transverse placement accuracy.

Object placement is more critical in the *z* dimension where even slight variations can create significant phase shifts. Coarse *z* placement is accurate to approximately 100 μm and is done by adjusting the object position until it is well focused when viewed through the long-distance microscope. Fine adjustment in *z* is done by observing the temporal location of the amplitude peak in the spatial sample waveform. The object's *z* position is adjusted until this peak coincides with the peak of the previously recorded reference waveform as shown in Fig. 6. In this way, the ranging capabilities of the system permit *z* positioning accurate to approximately 15 μm, or 1/10th of a wavelength for 2.0 THz. Therefore, with proper object placement, the multiple images are coherently locked together in phase. It is noted that these fine adjustments to the object position are always performed between image recordings to ensure that all the images have the proper phase relationship.

Successful AS also depends on temporal phase coherence among the spatial samples within a single image. Temporal coherence is limited by the precision of the motorized delay stepper, which is approximately 0.5 μm. This translates into 3.33 fs of temporal precision from scan to scan, far better than required.

Unlike most AS systems, the final higher-resolution, phased-array image is constructed by simply adding the multiple individual images. No mathematical reconstruction, deconvolution, or processing procedures are necessary since the AS essentially forms a single, sparse-aperture mirror. Furthermore, the mirror itself reconstructs the image in front of the receiver so the image itself is sampled, not just the scattered wave front. This represents a significant advantage over many other AS systems, such as those used in radio astronomy. In such systems, individual phased-array elements cannot be placed in a fashion to construct a single, coherent, sparse-aperture optic. Rather, individual movable elements are used to sample a wave front, which must then be reconstructed into an image by interferometric techniques.[31] Airborne SAR methods, for example, collect scattered wave-front data with a single array element that is scanned through the sky on an airplane. The data, known as the phase history,[32] is recorded and images are later reconstructed with numerical or optical techniques.

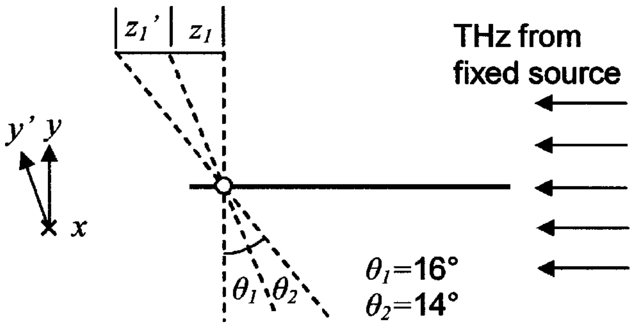

Fig. 7. Side view of the artificial aperture doubling model.

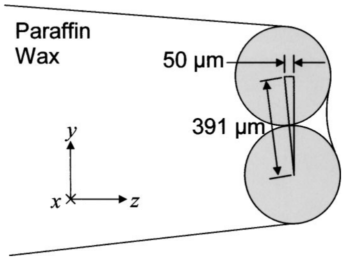

Fig. 8. Double 391-μm ball object for arrayed imaging.

The THz system, therefore, incorporates the power of large aperture optical imaging, commonly absent in AS systems, with the coherent properties common to microwave and radiowave systems. This blend makes high-resolution imaging at THz frequencies simple yet effective.

In a previous paper[7] we demonstrated the feasibility of synthetic phased-array THz imaging by imaging a 1-mm diameter, chrome-plated steel ball. Two individual images, designated E_1 and E_2, were recorded and superposed to form the higher-resolution composite image. Since the aperture was effectively increased in size only in the y direction, the overall effect of this imaging technique was a resolution increase of approximately four times in the (vertical) y direction. No resolution increase was evident in the x direction.

We note that we expected a resolution gain of two times, based on the 16° tilt between scan planes. However, the data revealed a resolution gain of four times because of an effect called artificial aperture doubling wherein the increase in the synthetic aperture size was approximately doubled because of the excess path length traveled by the illuminating THz. To explain this further, we first note that, in the xy plane, the arrival time of the illumination pulse to the object was approximately independent of the object's y position. However, in the tilted xy' plane, the illumination encountered more or less path length as the object scanned in the $+y'$ or $-y'$ directions, respectively. Figure 7 shows that, for a self-luminous object, the scan plane tilt would cause a path change of z_1. For the actual system, however, the illumination must also travel this extra path, which can be modeled as $z_1' = z_1$. This effectively adds an additional tilt of $\theta_2 = 14°$ to the original $\theta_1 = 16°$. The final effects are a scan plane tilt of 30° (an approximate doubling of the phased-array aperture size) and a resolution increase of four times over the nonarrayed imaging, to our advantage.

For AS in the vertical direction, the doubling effect is constrained to the y dimension, so it is independent of the time delays in the image caused by the angled illumination. For AS in the horizontal direction, the artificial aperture doubling still occurs but is superimposed on the time delays caused by the angled illumination. Finally, we note that the approximate doubling is only evident at small scan plane tilts (<20°) and, as tilt angles increase, the effect diminishes.

Another important result from the previous work[7] was the identification of several methods whereby 3-D image data can be plotted. One method is to integrate the time dimension by plotting the energy density of the images $G(x, y)$ rather than their field amplitudes, where

$$G(x, y) = \frac{1}{\eta_0} \int (E_1 + E_2 + E_3 + \ldots + E_n)^2 \mathrm{d}t. \quad (1)$$

Here, η_0 is the impedance of free space, E_1 through E_n represent the individual electric-field image data and their sum obviously represents their superposition. Therefore $G(x, y)$ is the composite energy image and contains both the interference terms and the individual energy density images $G_1(x, y)$ through $G_n(x, y)$ defined as

$$G_n(x, y) \equiv \frac{1}{\eta_0} \int E_n^2 \mathrm{d}t. \quad (2)$$

The net result is a two-dimensional image that would be obtained if THz photographic film or a THz CCD camera were placed in the image plane and used to record the image. These energy density images proved to be an important part of interpreting image data from the THz system.

To further demonstrate the enhanced capabilities of the system in the new research reported here, two 391 ± 3-μm-diameter, chrome-plated steel balls were mounted together to form the double point source object

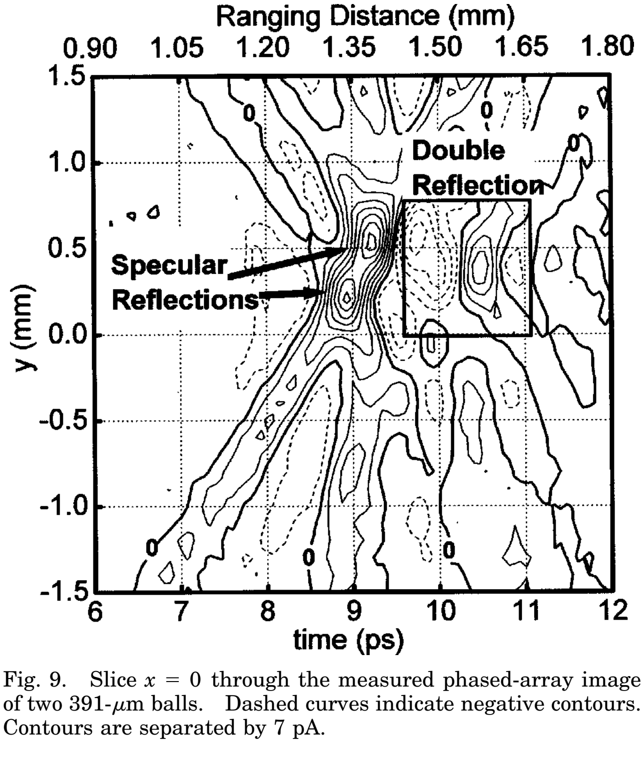

Fig. 9. Slice $x = 0$ through the measured phased-array image of two 391-μm balls. Dashed curves indicate negative contours. Contours are separated by 7 pA.

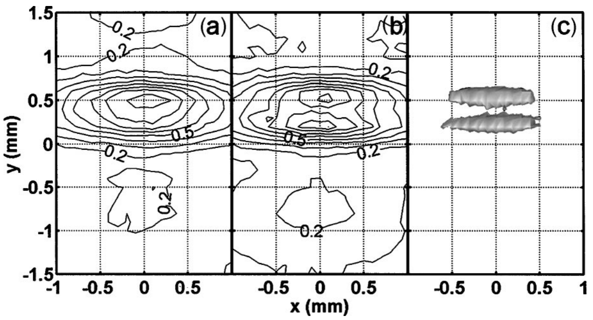

Fig. 10. Measured transverse images of two 391-μm balls: (a) total integrated energy density image, (b) partial integrated energy density image with double-reflection excluded; (c) isoamplitude image whose surfaces contain data values having an amplitude greater than 40 pA (80% peak).

shown in Fig. 8. The successful imaging of this object verified the resolvability of individual features on a more complex structure and determined some higher-order effects that interfere with phased-array imaging.

To reduce the possibility of large side lobes that obscure the final image (a result of sparse-aperture filling in phased-array systems), the aperture was filled in by recording three images rather than two, as in the initial demonstration.[7] The first image was recorded with the scan plane in the 0° orientation. The second and third images were recorded with the scan plane tilted $-10°$ and $+10°$ about the x axis, to mimic a synthetic mirror located below and above the spherical mirror, respectively.

Spatial samples were taken in both the x and the y directions so the resulting data set had the form $E(x, y, t)$. In all three images a total of 651 spatial samples were recorded: 31 samples in y by 21 samples in x. Spatial sample spacing was 100 μm in both directions so the image spanned a total of 2 mm in x and 3 mm in y. Each spatial sample was a 17-ps, time-dependent waveform that consisted of 256 data points. The peak SNR of the data was approximately 120. All three individual images were superposed to generate the higher-resolution composite image.

Figure 9 shows an $x = 0$ volumetric slice through the composite image data of the two balls. The balls are resolved in the y direction and, because of their close proximity, to a lesser extent in the t (or z) direction. Also evident is a double reflection feature that occurs later in time. This feature is the multipath effect, wherein the THz is first reflected from one ball to the next and then to the receiver. The double reflection feature becomes important when viewing the transverse images, because it interferes with the resolvability of the balls. Consider the energy density image of the two balls shown in Fig. 10(a). This image was created by applying Eq. (1) to the data where the integration included the entire temporal span of the image. Although it is weaker, the double reflection is situated right between the two specular reflections and acts as clutter in the transverse image. The specular features are blended together by the double reflection, and the resolution of the balls is destroyed. This illustrates the important fact that, even though an imaging system is well corrected and its diffraction limit is low enough to resolve two objects properly, they still might not be resolvable because of higher-order effects. Such higher-order effects would be even more significant in imaging more complicated objects, where several multipath effects could be simultaneously observed.

These images also demonstrate the added power of coherent over incoherent imaging systems. An incoherent system could neither resolve the two balls in range nor in transverse space. However, in the coherent THz system, the resolution in range is excellent and further permits the removal of the double reflection feature that occurs later in time. By excluding the data that contain the double reflection ($t > 9.6$ ps) from the integration, the detrimental effect is removed. Figure 10(b) shows the same energy density image as Fig. 10(a) after time excluding the double reflection feature. The resolvability of the balls reappears in the transverse image.

Other image-processing methods can be used to reveal the resolution between the two balls. Figure 10(c) shows one example wherein the image data were processed in a binary fashion such that only values of sufficient amplitude were retained and all the other values were discarded. The transverse image of the two balls is then plotted as the surface of the volume that contains the retained values. In this case the threshold amplitude was 80% of the peak value. This method removes the double reflection features while retaining the stronger, specular features. Figures 10(b) and 10(c) both show that the resolution in the y direction has increased by 4.5 to 5 times, whereas the resolution in the x direction is unchanged, as expected.

The images of Fig. 10 demonstrate a few of the image-processing and enhancement techniques available to this system by digitally storing the coherent, phase-locked individual images. Such techniques permit imaging of smaller or less reflective objects, imaging of objects in clutter, and filtering of undesired features. Unwanted image anomalies, often distinguished by later arrival, weaker amplitude response, and/or altered spectral response, can be easily removed by temporal feature exclusion, amplitude thresholding, and frequency filtering in both the temporal and the spatial domains. These image-processing and enhancement techniques show the power and flexibility of the synthetic phased-array THz imaging system.

Other signal-processing techniques have also been applied to THz systems to retrieve information from compli-

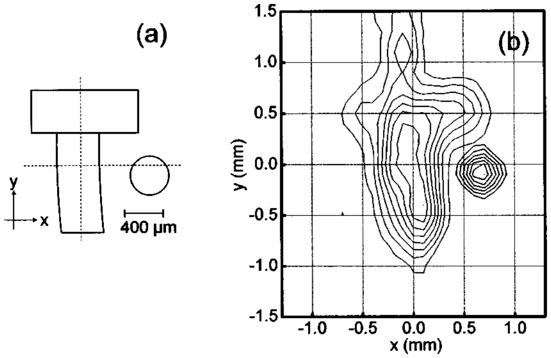

Fig. 11. (a) Scale diagram of the T-ball object. Dashed lines indicate the center of the data set. (b) Overlap of separately normalized partial energy density images of T and ball. Contour at 0.3 removed from the ball image. Contours at 0.1 and 0.2 removed from both images.

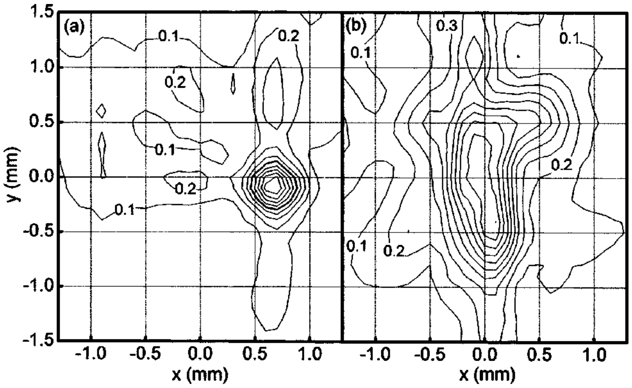

Fig. 12. Measured partial energy density images of T-ball object, both separately normalized. Contour separation is 0.1: (a) image of ball, heavy contour indicates the half-maximum and (b) image of T.

cated scattering events. Tomographic processing has been applied with success to THz imaging[13] and can be used to identify multiple dielectric interfaces in complex objects by means of digital signal processing. THz ranging that utilizes ultrawideband radar techniques has been used to identify electromagnetic scattering events in dielectric objects.[33] Other inverse techniques such as the Kirchhoff migration have been used to generate THz images of buried objects.[30] Such work provides many tools for image processing that would likely be partially applicable in our THz imaging system.

In one final demonstration of the system's capabilities, arraying was performed in both the x and the y directions. The object used for this experiment was a small metallic T positioned next to a 391-μm steel ball, as shown in Fig. 11(a). The T was constructed from two cylindrical pieces of solder, each having a diameter of approximately 420 μm. The T portion lay in the plane perpendicular to the system optical axis (z axis).

The ball was mounted approximately 260 μm closer to the spherical mirror in the z direction so it was temporally resolved from the T. Five images of this object were recorded; the first was recorded with the scan plane in the normal orientation or 0° tilt. The second and third images were recorded with the scan plane tilted $+10°$ and $-10°$ about the y axis to mimic synthetic mirrors located to the left ($-x$ direction) and right ($+x$ direction) of the real mirror, respectively. The fourth and fifth images were recorded with the scan plane tilted $+10°$ and $-10°$ about the x axis to mimic a synthetic mirror located above and below the synthetic mirror, respectively. Spatial samples were taken in both the x and the y dimensions so the resulting data had the form $E(x, y, t)$. In each of the five images a total of 837 spatial samples were recorded: 31 samples in y by 27 samples in x. Spatial sample spacing was 100 μm in both directions so that the image spanned a total of 2.6 mm in x and 3.0 mm in y. Each spatial sample was a 17-ps time-dependent waveform that consisted of 256 data points, each spaced by 66.7 fs. The peak SNRs of the images ranged from 25 to 100, depending on the object orientation. All five images were superposed to form the single, higher-resolution composite image.

Even though multipath effects were not a problem with this object, it was determined that partial energy density images would yield the best visualization. The separate images of the ball and the T are shown in Figs. 12(a) and 12(b), respectively. These images were obtained by splitting the data into two sections. The first section contained all the data within the time window of $t = 0$–5.6 ps, and thus included only the reflection from the ball. The second section contained data within the window of $t = 5.6$–17 ps, and thus contained only the reflections from the T. Each section of field data was squared and integrated separately. This resulted in two partial energy density images, one containing the ball and the other containing the T. The ball is clearly resolved in Fig. 12(a) and shows that the phased-array imaging was successful in both the x and the y directions. The FWHM measurement of the ball in this energy picture is approximately 435 μm in both the x and the y directions, indicating a resolution increase of approximately 4.25 times. The T also exhibits features evident only because of the increased resolution.

Again, these two images were separately normalized, so even though contours may have the same label, they do not correspond to the same intensity. The T, having cylindrical surfaces, reflected more THz radiation than the ball, so its energy density image was approximately eight times stronger. This is part of the reason the ball and T were plotted separately and partial time integration was used. A full time integration would have rendered the ball almost invisible against the much more strongly reflecting T.

The two separately normalized images can be overlapped to view the whole object at once as shown in Fig. 11(b). Again, the two images were not added but simply overlapped. Some contours were removed from each picture to clarify the image, and no contour labels are shown since they correspond to different absolute values. Nevertheless, the image clearly reproduces the object, shown in Fig. 11(a) with the same scale, quite well.

Figures 11(b) and 12(b) also show a reduced fidelity in the top (horizontal) portion of the T, as compared with the bottom. This effect is due to the cylindrical surfaces of the T that, unlike the spherical ball surfaces, do not reflect the off-axis illumination in every direction. Both portions of the T lie in a plane perpendicular to the system optic axis so that in the normal scan plane configuration (0° tilt), the top portion of the T reflects the THz as a horizontal cylindrical wave spreading in a direction that does not coincide with the spherical mirror. However, the bottom portion reflects a vertical cylindrical wave that compensates for the off-axis illumination and thereby intersects the mirror. This stealth behavior is present in any object with flat features. As the object tilts with the reoriented scan plane, this problem can be either exacerbated or subdued. Tilts about the y axis affect horizontally flat features, whereas tilts about the x axis affect vertically flat features. This allowed the horizontal portion of the T to be strongly visible in only one of the five total images recorded. The tilted orientations about the x axis caused the vertical portion to become less visible in two of the five images. Of course, the spherical ball was visible in all five images.

To rule out other explanations for the visibility of the T, the xz plane polarization of the illuminating THz was also considered. The polarization effect, however, was deemed insignificant with respect to geometric considerations because polarization dependence would be predominantly manifest in weak creeping waves that couple more favorably onto one component of the T. The pulsed THz system would resolve such waves later in time and at significantly lower amplitudes than specular reflections. Although such waves would be generated on both cylindrical and spherical objects, no such waves of significant amplitude were ever observed in the relevant time window. This is likely due, in part, to the fact that the backs of the objects are mounted in wax, which both slows and attenuates the creeping waves.

Two issues of relevance to the practicality of this system are imaging acquisition times and measurement stability. To achieve the clear measure of range resolution presented in these images, individual data points in each time-domain scan were separated by no more than 66.7 fs. This sampling rate provided excellent temporal fidelity of the waveform and usable frequency information to 7.5 THz. However, such a high sampling rate requires many data points to fill the necessary time window encompassing the scans, and, at this rate, individual time-domain scans required approximately 1.5 min to complete. One-dimensional images having between 41 and 61 scans were recorded in approximately 1–1.5 h. By simply decreasing the sampling rate from 15 to 5 THz, this imaging time could be reduced by three times, without loss of frequency information. Further duration reductions, by several orders of magnitude, could be made by decreasing the amount of averaging performed by the lock-in amplifier or by using rapid-scan techniques.[11] Such reductions are commonly necessary in THz imaging systems but come at the cost of SNR; therefore they justify further research into stronger THz sources and more sensitive receivers.

Two-dimensional and phased-array imaging obviously present a greater challenge because of the necessarily larger number of scans to record. Rapid-scan techniques would almost certainly be required to generate these large images quickly but would likely yield imaging times of the order of minutes rather than days. Such changes are not difficult to implement on the THz system but do currently pose problems in terms of SNR for small objects.

Finally, the fact that imaging duration is quite long accentuates the excellent stability inherent in our THz imaging system. Even for large, phased-array data sets, imaging can continue essentially indefinitely without concern for maintaining phase coherence. Although this is due mostly to the natural stability of laser and THz systems, it is also due to the fact that we record occasional reference scans to identify slow signal drift. This allows slight adjustments to be made if necessary.

5. THEORY

The theoretical analysis of this THz imaging system can be accurately performed with a hybrid method of geometrical optics and diffraction theory. Geometrical optics, or ray tracing, is used to determine a field distribution in or near a certain plane that contains the exit pupil. From this point, diffraction theory is used to propagate the field to the image plane. This hybrid method is well known[34] and has the benefits of simplicity, high accuracy, and relative completeness, because of the inclusion of most imaging effects such as third-order aberrations and diffraction. Since we use a scalar diffraction theory, the vectorial nature of the fields is ignored.

As described in Section 2, the THz imaging system consists of two separate imaging subsystems. In the first subsystem, the spherical mirror forms an intermediate image of the object in a plane located 17 mm in front of the receiver. In the second subsystem this intermediate image is once again imaged onto the receiver dipole antenna by the silicon lens mounted in the receiver. It was found that the second subsystem behaved as a nearly ideal sampler of the intermediate image and did not introduce any additional effects over those present from the spherical mirror. Therefore to model the entire THz system we needed to include only the imaging of the object by the spherical mirror. This approach had the added utility of returning results of the same form as the data.

To maintain consistency with the optics references[35–37] from which most of the THz imaging system theory comes, we chose a phasor notation such that phasors rotate in a clockwise direction as time moves forward. Equivalently, their time dependence has the form $\exp(-j\omega t)$, where j represents the unit imaginary number, ω is the angular frequency, and t is time. By use of this phasor notation, the Fourier transform and its inverse must be expressed as

$$F(\omega) = \int_{-\infty}^{\infty} f(t)\exp(j\omega t)\mathrm{d}t, \tag{3}$$

$$f(t) = \frac{1}{2\pi}\int_{-\infty}^{\infty} F(\omega)\exp(-j\omega t)\mathrm{d}\omega. \tag{4}$$

In this notation a diverging spherical wave takes the form $\exp(jkr)/r$. As a point of caution, these notations have a reversed sign from common electrical engineering references, wherein phasors have the time dependence of $\exp(j\omega t)$.

The theoretical model begins in the frequency domain with an object located at some point O, as shown in Fig. 13. The object is assumed to be a point source that emits an isotropic, diverging spherical wave. This wave is represented in geometrical-optics fashion by a bundle of rays

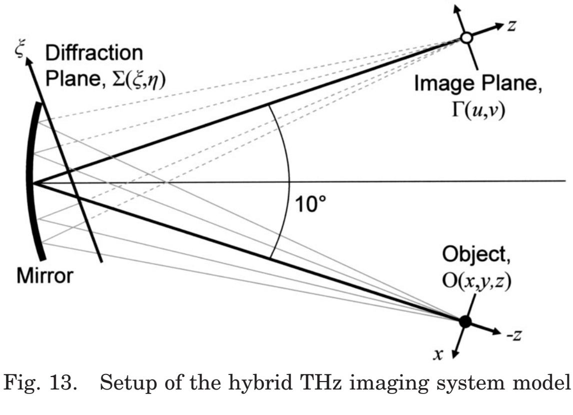

Fig. 13. Setup of the hybrid THz imaging system model.

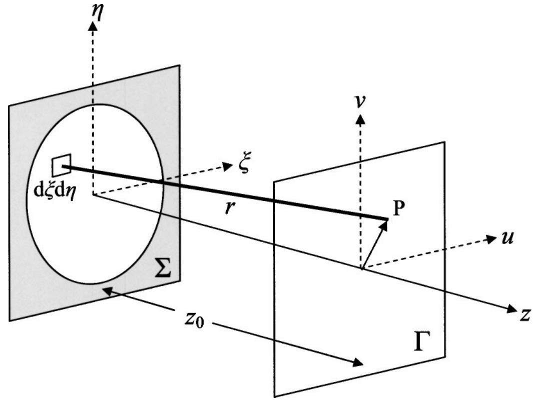

Fig. 14. Setup for the diffraction portion of the calculation.

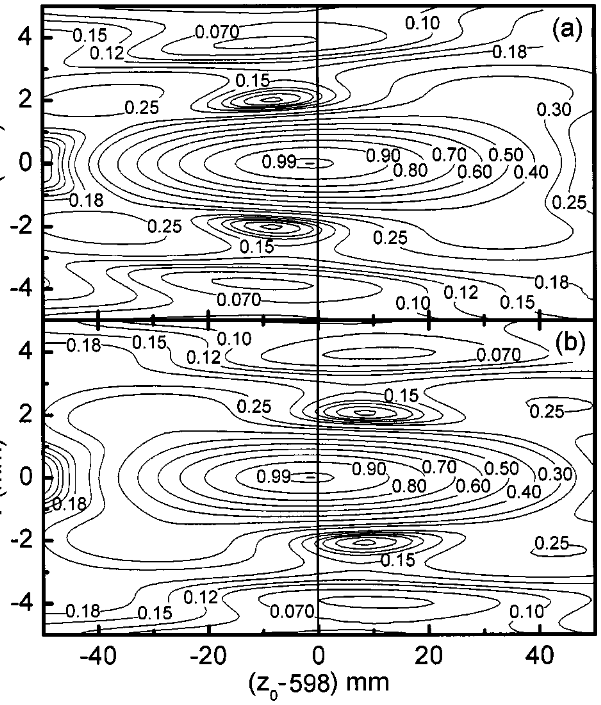

Fig. 15. Normalized field magnitude slices of the theoretical point source image at 0.7 THz: (a) $v = 0$ slice and (b) $u = 0$ slice.

that propagate toward the spherical mirror. The rays are incident upon and reflected by the mirror, then intersect diffraction plane Σ. Rays that do not intersect the mirror are not reflected to the diffraction plane so the extent of the mirror is automatically projected onto Σ, thus defining the exit pupil.

All the rays are mathematically represented by 3-D vectors. We calculated the reflected rays by rotating the incident ray vectors 180° about the surface normal vectors at the incidence points. The location of each reflected ray and the overall distance it has traveled when it intersects with Σ is then calculated with basic vector principles. This distance is assigned the variable name Δ, consistent with Ref. 35. More explicitly, $\Delta = \Delta(\xi, \eta)$ is a function of spatial position. The spatially varying phase distribution over Σ can then be defined by $\exp(jk\Delta)$, where k is the wave number equal to $2\pi/\lambda$ and λ is the free-space wavelength. All the rays from the source are assumed to have the same strength at Σ, therefore the entire field distribution, with both amplitude and phase, is known therein. We designate this field distribution in the frequency domain as $U(\xi, \eta, \omega) = \exp(jk\Delta)$. Since $\exp(jk\Delta)$ specifies all the phase information of the field at the diffraction plane, all the effects of imaging aberrations are contained within the Δ variable.

Using $U(\xi, \eta, \omega)$, the field distribution in the geometric image plane can be calculated. We used the setup shown in Fig. 14 and the first Rayleigh–Sommerfeld diffraction integral[35]

$$H_\Gamma(u, v, \omega) = \frac{z_0}{j\lambda} \iint_\Sigma U(\xi, \eta, \omega) \frac{\exp(jkr)}{r^2} \mathrm{d}\xi \mathrm{d}\eta. \tag{5}$$

In Eq. (5) z_0 is the z dimension distance between the diffraction and the image planes. The variable r is the distance between the differential field element $\mathrm{d}\xi\mathrm{d}\eta$ located at (ξ,η) and the observation point P located at (u, v), and it therefore has the explicit dependence $r = r(u, v; \xi, \eta)$. Since the source is a point radiator, $H_\Gamma(u, v, \omega)$ represents the frequency domain PSF of the imaging system.

We note here that the spatial variables used throughout the theory, (x, y), (ξ, η), and (u, v), have been chosen to maintain consistency with Ref. 35. However, to preserve continuity with the experimental setup, the object and diffraction plane coordinates are designated (x, y) and (ξ, η), respectively. This notation is reversed in Ref. 35. The scale relationship between all the spatial variables is one to one. Therefore, theoretical images with (u, v) dependence can be directly compared with experimental images with (x, y) dependence.

Incorporating the previous definition of $U(\xi, \eta, \omega)$ into Eq. (5) gives the final form of the PSF:

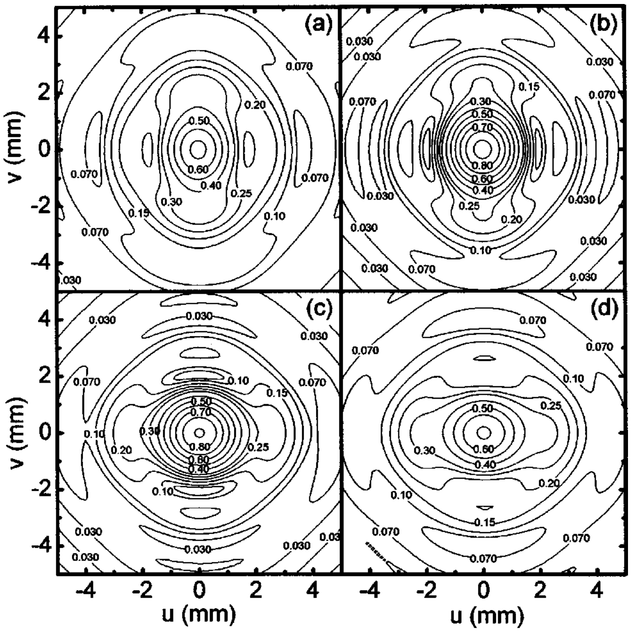

Fig. 16. Normalized transverse slices through the theoretical point source image at 0.7 THz: (a) $z_0 = 574$ mm, (b) $z_0 = 586$ mm, (c) $z_0 = 610$ mm, (d) $z_0 = 622$ mm.

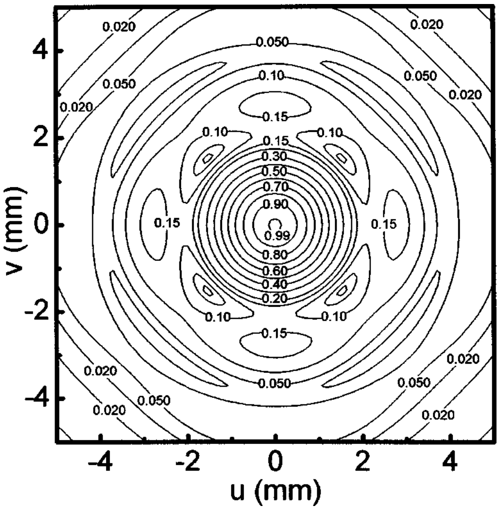

Fig. 17. Normalized transverse COLC field magnitude slice through the theoretical point source image at 0.7 THz; $z_0 = 598$ mm.

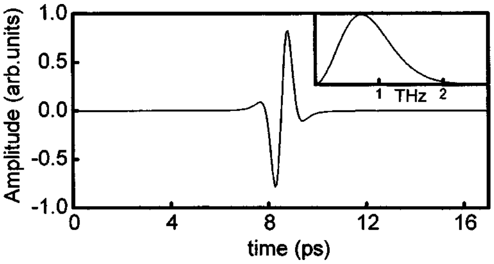

Fig. 18. Ideal input pulse for theoretical calculations. Inset shows the normalized amplitude spectrum.

$$H_\Gamma(u, v, \omega) = \frac{z_0}{j\lambda} \iint_\Sigma \frac{\exp[jk(r + \Delta)]}{r^2} \mathrm{d}\xi \mathrm{d}\eta. \tag{6}$$

The final calculation is performed numerically and without any further approximations to the phase or amplitude. All the calculations are set up to match the physical dimensions of the actual system.

Several theoretical images were calculated with Eq. (6) for 0.7 THz. Since the object is a point source, the resulting image is nearly equivalent to a diffraction-limited focus of the spherical mirror. Therefore, the image can also be thought of as a focal region. To describe the structure of this calculated focal region, Fig. 15 shows two orthogonal slices calculated for several values of z_0 in the area around the geometric image plane. These field magnitude plots clearly show the elongated, tubular structure of the focal region (the image) in the z direction. This structure is common to focusing systems and provides a considerable tolerance in the positioning of the image plane,[37] or the receiver, in our case. This tolerance is greater than 10 mm for the THz system and has been verified with experiments.

As is obvious in the figures, the focal region is not rotationally symmetric about the z axis predominantly because of astigmatism. Figure 16 shows some transverse images through this focal region to illustrate this fact further. As expected from geometrical optics, the primary image, also called the tangential line focus, is vertical in orientation and lies nearest to the spherical mirror. The secondary image, also called the sagittal focus, is horizontal in orientation and lies farthest from the spherical mirror. Between these two foci lies the plane that contains the circle of least confusion (COLC), where imaging is most correct. Figure 17 shows that the image in this plane has the expected general features of a diffracted astigmatic image as shown in Section 9.4.3 of Ref. 37. To ensure the validity of our calculations against those of Refs. 37, 38, and Section 5.3.1 of Ref. 35, they were also performed with the 10° off-axis orientation of the system reduced to 0°. The results of these on-axis calculations were found to be a good match with the references and can be found in Ref. 22.

Equation (6) can be multiplied by the complex spectrum of the broadband THz pulse $S(\omega)$ to give the frequency domain form of broadband image $U_\Gamma(u, v, \omega)$:

$$U_\Gamma(u, v, \omega) = S(\omega) H_\Gamma(u, v, \omega). \tag{7}$$

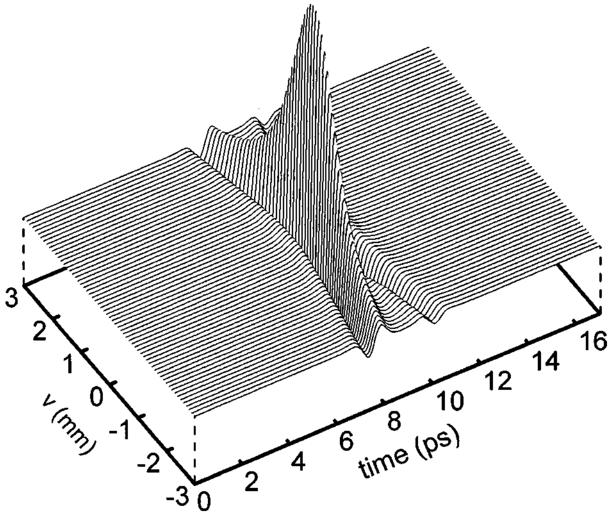

Fig. 19. Broadband $u = 0$ slice through the theoretical image of the point source.

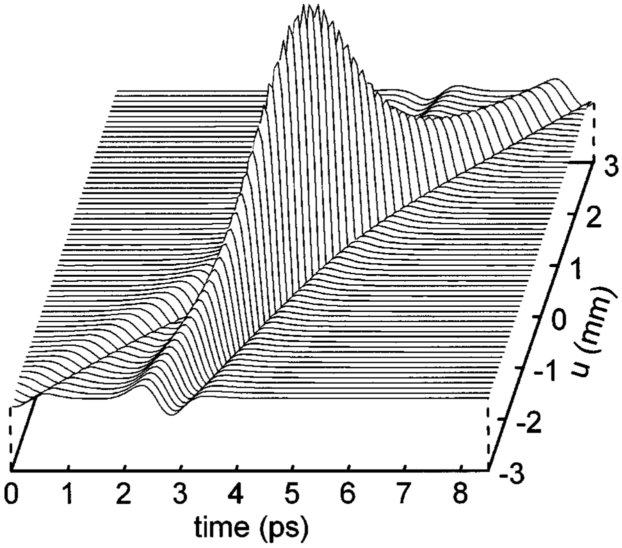

Fig. 20. Broadband $v = 0$ slice through the theoretical image of the point source with the corrected illumination effect.

The time-domain broadband image $U_\Gamma(u, v, t)$ can then be calculated by use of the inverse Fourier transform

$$U_\Gamma(u, v, t) = \frac{1}{2\pi}\int_{-\infty}^{\infty} S(\omega)H_\Gamma(u, v, \omega)\exp(-j\omega t)\mathrm{d}\omega. \tag{8}$$

To clean up the theoretical images, an idealized THz pulse was used as the input $S(\omega)$. This pulse was modeled after an actual recorded THz pulse, similar to those shown in Fig. 6, but given a frequency-independent phase shift of $-\pi/2$, relative to the pulse in Fig. 6. This offsets the $\pi/2$ phase shift introduced by the theory as the diffracted radiation propagates from the mirror to the image plane. This term is manifest as the $1/j$ in Eqs. (5) and (6). Application of the $-\pi/2$ shift to the input pulse does not compensate for a theoretical deficiency but merely ensures that the input to the theory is properly defined. The resulting input pulse and its spectrum are shown in Fig. 18.

Figure 19 shows a $u = 0$ slice through the two-dimensional broadband image of a point source. Unlike the monochromatic images, this image is calculated in only one image plane, positioned at the COLC, $z_0 = 598$ mm. To this point, no account has been taken of the fact that the object is not self-luminous in the actual system. The only significant effect of the angled illumination is the angled appearance of the image with respect to the x axis, which is caused by a slight shifting of the spatial samples in time. The obvious accounting for this phenomenon is to shift each spatial sample temporally in the theoretical image. The shift amount is determined by noting that, at the object, the illumination beam is effectively planar, and that as the object moves δx in the $+x$ direction it moves nearer to the transmitter by the amount $\delta x \sin(17°)$. The illumination travels at c, therefore the temporal shift of each spatial sample is $\delta x \sin(17°)/c = \delta x \times 0.975$ ps/mm, where δx is expressed in millimeters. Because of the sampling nature of the system, as the object moves in the $+x$ direction, the receiver samples the $-x$ side of the image. Therefore, positive and negative δx translate into shifts later and earlier in time, respectively. Since u and x are equivalent in scale, shifting the theoretical spatial samples by the amount prescribed yields the new broadband image shown in Fig. 20. Only the $v = 0$ slice image is shown because the angled illumination does not affect the image in the v direction. Figure 20 shows the final form of the theoretical image of a point source: the broadband PSF. The agreement between theory and data is good as shown by comparing Fig. 20 with the actual image recorded by the system shown in Fig. 4(a).

Another calculation was performed with a halved diameter spherical mirror to model the halved mirror experiment explained earlier. Again, the hybrid model was a good match with experiment and produced an image with a 1.72 times increase in spatial width, which indicates that the system behavior and theoretical calculations are in good harmony. Furthermore, since the secondary imaging system in the receiver is not included in the theory, it reinforces the assumption that the receiver has a minimal effect on imaging.

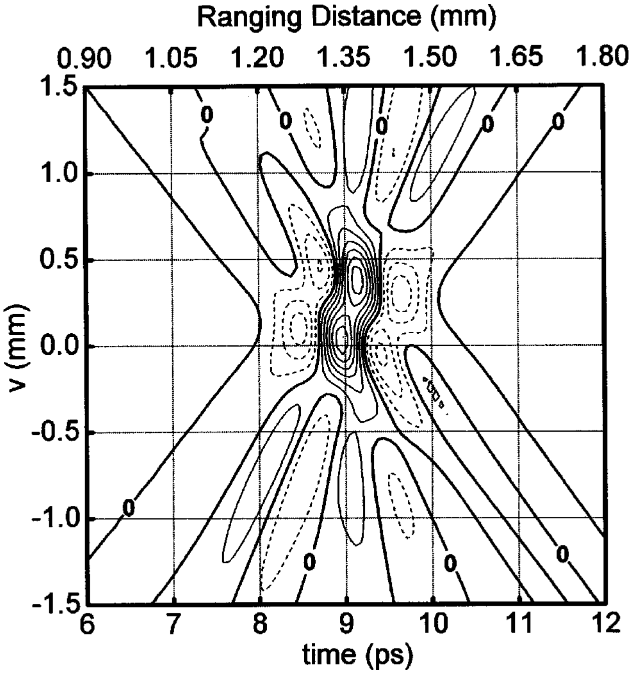

Fig. 21. Slice $u = 0$ through the normalized theoretical arrayed image of two point sources separated by 400 μm in y and 50 μm in z. Contour separation is 0.15. Dashed curves indicate negative contours. The image was shifted -200 μm in v compared with Fig. 9.

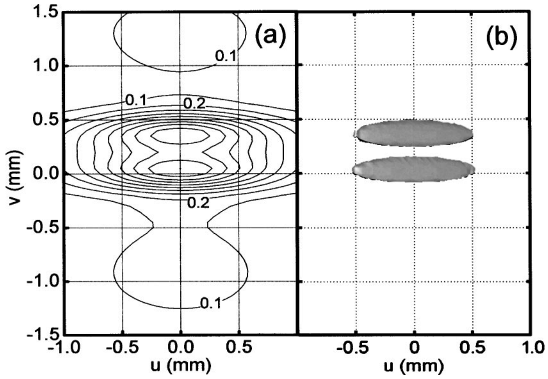

Fig. 22. Theoretical transverse image of two point sources: (a) energy density image and (b) iso-amplitude image where plotted surfaces contain data values where the electric-field amplitude is greater than 80% of the maximum. Both images were shifted -200 μm in v compared with Fig. 10.

The image calculations must be discretized to be performed, so it is worthwhile to discuss their validity. The discretization necessitates a trade-off between accuracy and speed, so for most of our calculations we propagated a bundle of rays that formed a spatial grid of 151 × 151 points over the face of the spherical mirror. Even though this grid density is not strictly sufficient to map the phase distribution unambiguously over the diffraction plane at higher frequencies (>1.5 THz), it was found to yield results with good accuracy and reasonable calculation times of the order of 10–15 min for a two-dimensional broadband image by use of a 2.8-GHz processor. However, to ensure accurate results, additional monochromatic and broadband calculations were performed with grids of 351 × 351 up to 2 THz. This grid density provides at least two data points per each oscillation of the phase distribution of the wave front over the diffraction plane, even at 2 THz. For lower frequencies, this condition is improved. We found that calculations using the 151 × 151 grid size were a good match with larger grid results. Additionally, since a large portion of the THz bandwidth exists at lower frequencies centered around 0.7 THz, even smaller grid sizes, down to 51 × 51, still produced similar broadband results. It is not surprising that the THz system is well suited to such calculations because the relatively long wavelengths permit far fewer calculation points than would be necessary in a typical optical system. This provides vastly improved calculation speed and accuracy.

Phased-array imaging can also be theoretically modeled. Like the experimental procedure, theoretical image arraying requires only the superposition of individual images. Unlike the actual system, however, the theory does not necessitate scanning the object to form the image. Therefore, some other accounting must be made for the timing shifts induced by scanning the object in a tilted plane. Note that the object is scanned in a tilted plane to achieve the effects of a synthetic mirror, and that the scan plane has a slight z dependence when it is tilted about either the x or the y axis. Therefore, most of the spatial samples of an arrayed image are recorded when the object has some nonzero z location. For small angular separations ($<20°$ disregarding artificial aperture doubling) between array elements this z motion can be neglected with respect to its effect on the transverse spatial field distribution because the elongated focus significantly desensitizes this dependence. However, this same z motion must be accounted for in timing, and this can easily be done by the same method that was used to account for the angled illumination. Simple time delays are appropriately added to the spatial samples depending on their x and y positions and the desired angular separation between array elements. This method is easily incorporated into the timing shifts caused by the angled illumination. Note that, in these experiments, this caused an effective doubling of the overall phased-array aperture size. The same is true for the theory.

For comparison with actual data, the theoretical arrayed image of two point sources was calculated. The sources were separated by 400 μm in y and 50 μm in z to mimic the imaging of the two abutting 391-μm balls shown in Fig. 8. Arraying was done in the vertical direction only, and array orientations were 0°, +10°, and −10°, just as in the experimental data. Again, the theory corrects the timing effects of the angled illumination and the ranging nature of the system, but only after assuming a self-luminous object for the diffraction calculations. Since there is no illumination in the theory, there is also no multipath effect manifest as a double reflection. Figures 21 and 22 show the calculated array images for this object. They compare quite well with the actual images shown in Figs. 9 and 10.

6. CONCLUSIONS

We have demonstrated a quasi-optic, synthetic phased-array THz imaging system that can produce THz images sharp enough to resolve features whose size is of the order of a wavelength or less in all three dimensions. This system utilizes the benefits of phase coherence to achieve synthetic aperture imaging similar to microwave and radiowave techniques. However, it simultaneously produces individual, high-resolution images in an optical fashion. This dual nature greatly enhances high-resolution THz imaging in terms of both speed and sensitivity. It also permits the system to form resolved images of objects that would otherwise be unresolvable in an incoherent system, because of higher-order effects such as multiple-scattering events. Furthermore, the system can be accurately modeled by common optical principles yet can be more easily adapted to numerical computation because of longer wavelengths and the accompanying relaxed accuracy restrictions.

Such an imaging system promises application in many types of noninvasive imaging arena for which microwave techniques do not offer sharp enough resolution and optical techniques suffer from opacity or optical sensitivity problems. Although usable SNRs require long imaging durations to record large composite AS images, ongoing research in stronger THz sources will eventually allow this type of imaging to be adapted to a real-time setting, thus increasing its applicability beyond static objects.

This research was partially supported by the National Science Foundation and the U.S. Army Research Office. D. Grischkowsky's e-mail address is grischd @ceat.okstate.edu.

REFERENCES

1. D. H. Auston, K. P. Cheung, and P. R. Smith, "Picosecond photoconducting Hertzian dipoles," Appl. Phys. Lett. **45**, 284–286 (1984).
2. M. B. Ketchen, D. Grischkowsky, T. C. Chen, C.-C. Chi, I. N. Duling III, N. J. Halas, J.-M. Halbout, J. A. Kash, and G. P. Li, "Generation of subpicosecond electrical pulses on coplanar transmission lines," Appl. Phys. Lett. **48**, 751–753 (1986).
3. B. B. Hu, X.-C. Zhang, D. H. Auston, and P. R. Smith, "Free-space radiation from electro-optic crystals," Appl. Phys. Lett. **56**, 506–508 (1990).
4. Q. Wu and X.-C. Zhang, "Free-space electro-optic sampling of terahertz beams," Appl. Phys. Lett. **67**, 3523–3525 (1995).
5. M. van Exter and D. R. Grischkowsky, "Characterization of an optoelectronic terahertz beam system," IEEE Trans. Microwave Theory Tech. **38**, 1684–1691 (1990).
6. K. McClatchey, M. T. Reiten, and R. A. Cheville, "Time resolved synthetic aperture terahertz impulse imaging," Appl. Phys. Lett. **79**, 4485–4487 (2001).
7. J. O'Hara and D. Grischkowsky, "Synthetic phased-array terahertz imaging," Opt. Lett. **27**, 1070–1072 (2002).
8. L. Thrane, R. H. Jacobsen, P. Uhd Jepsen, and S. R. Keiding, "THz reflection spectroscopy of liquid water," Chem. Phys. Lett. **240**, 330–333 (1995).
9. J. T. Kindt and C. A. Schmuttenmaer, "Far-infrared dielectric properties of polar liquids probed by femtosecond terahertz pulse spectroscopy," J. Phys. Chem. **100**, 10373–10379 (1996).
10. M. P. van Exter, C. Fattinger, and D. Grischkowsky, "Terahertz time-domain spectroscopy of water vapor," Opt. Lett. **14**, 1128–1130 (1989).
11. D. M. Mittleman, R. H. Jacobsen, and M. C. Nuss, "T-ray imaging," IEEE J. Sel. Top. Quantum Electron. **2**, 679–692 (1996).
12. B. B. Hu and M. C. Nuss, "Imaging with terahertz waves," Opt. Lett. **20**, 1716–1718 (1995).

13. D. M. Mittleman, S. Hunsche, L. Boivin, and M. C. Nuss, "T-ray tomography," Opt. Lett. **22**, 904–906 (1997).
14. Q. Wu, T. D. Hewitt, and X.-C. Zhang, "Two-dimensional electro-optic imaging of THz beams," Appl. Phys. Lett. **69**, 1026–1028 (1996).
15. Z. Jiang and X.-C. Zhang, "Single-shot spatiotemporal terahertz field imaging," Opt. Lett. **23**, 1114–1116 (1998).
16. J. O'Hara and D. Grischkowsky, "Quasi-optic terahertz imaging," Opt. Lett. **26**, 1918–1920 (2001).
17. N. Katzenellenbogen and D. Grischkowsky, "Efficient generation of 380 fs pulses of THz radiation by ultrafast laser pulse excitation of a biased metal-semiconductor interface," Appl. Phys. Lett. **58**, 222–224 (1991).
18. A. J. den Dekker and A. van den Bos, "Resolution: a survey," J. Opt. Soc. Am. A **14**, 547–557 (1997).
19. A. B. Ruffin, J. Decker, L. Sanchez-Palencia, L. Le Hors, J. F. Whitaker, T. B. Norris, and J. V. Rudd, "Time reversal and object reconstruction with single-cycle pulses," Opt. Lett. **26**, 681–683 (2001).
20. J. L. Johnson, T. D. Dorney, and D. M. Mittleman, "Interferometric imaging with terahertz pulses," IEEE J. Sel. Top. Quantum Electron. **7**, 592–599 (2001).
21. S. Krishnamurthy, M. T. Reiten, S. A. Harmon, and R. A. Cheville, "Characterization of thin polymer films using terahertz time-domain interferometry," Appl. Phys. Lett. **79**, 875–877 (2001).
22. J. O'Hara, "Experimental study of a quasi-optic synthetic phased-array terahertz imaging system," Ph.D. dissertation (School of Electrical and Computer Engineering, Oklahoma State University, Stillwater, Okla., 2003).
23. M. Ryle and A. Hewish, "The synthesis of large radio telescopes," Mon. Not. R. Astron. Soc. **120**, 220–230 (1960).
24. P. J. Napier, A. R. Thompson, and R. D. Ekers, "The very large array: design and performance of a modern synthesis radio telescope," Proc. IEEE **71**, 1295–1322 (1983).
25. P. J. Napier, D. S. Bagri, B. G. Clark, A. E. E. Rogers, J. D. Romney, A. R. Thompson, and R. C. Walker, "The very long baseline array," Proc. IEEE **82**, 658–672 (1994).
26. A. Labeyrie, "Interference fringes obtained on Vega with two optical telescopes," Astrophys. J. Lett. **196**, L71–L75 (1975).
27. A. R. Haijan and J. T. Armstrong, "A sharper view of the stars," Sci. Am. **284**, 56–63 (2001).
28. A. Broquetas, J. Palau, L. Jofre, and A. Cardama, "Spherical wave near-field imaging and radar cross-section measurement," IEEE Trans. Antennas Propag. **46**, 730–735 (1998).
29. D. Mensa, *High Resolution Radar Imaging* (Artech House, Dedham, Mass., 1981).
30. T. D. Dorney, J. L. Johnson, J. Van Rudd, R. G. Baraniuk, W. W. Symes, and D. M. Mittleman, "Terahertz reflection imaging using Kirchhoff migration," Opt. Lett. **26**, 1513–1515 (2001).
31. J. D. Kraus, *Radio Astronomy* (McGraw-Hill, New York, 1966).
32. D. R. Wehner, *High Resolution Radar* (Artech House, Norwood, Mass., 1987).
33. R. W. McGowan, R. A. Cheville, and D. R. Grischkowsky, "Experimental study of the surface waves on a dielectric cylinder via terahertz impulse radar ranging," IEEE Trans. Microwave Theory Tech. **48**, 417–422 (2000).
34. J. J. Stamnes, *Waves in Focal Regions* (Adam Hilger, Bristol, England, 1986).
35. J. W. Goodman, *Introduction to Fourier Optics*, 2nd ed. (McGraw-Hill, New York, 1996).
36. E. Hecht, *Optics*, 4th ed. (Addison-Wesley, San Francisco, Calif., 2002).
37. M. Born and E. Wolf, *Principles of Optics*, 7th ed. (Cambridge University, Cambridge, England, 1999).
38. Y. Li and E. Wolf, "Three-dimensional intensity distribution near the focus in systems of different Fresnel numbers," J. Opt. Soc. Am. A **1**, 801–808 (1984).